Article:

Joo, H.-J. orcid.org/0000-0002-4923-9771, Liu, J., Chen, M. orcid.org/0009-0003-3201-9603 et al. (14 more authors) (2024) Actively tunable laser action in GeSn nanomechanical oscillators. Nature Nanotechnology. ISSN 1748-3387

https://doi.org/10.1038/s41565-024-01662-w

Actively tunable laser action in GeSn nanomechanical oscillators

Hyo-Jun Joo[1†], Jiawen Liu[2†], Melvina Chen[1†], Daniel Burt[1], Baptiste Chomet[2], Youngmin Kim[1], Xuncheng Shi[1], Kunze Lu[1], Lin Zhang[1], Zoran Ikonic[3], Young-Ik Sohn[4], Chuan Seng Tan[1], Djamal Gacemi[2], Angela Vasanelli[2], Carlo Sirtori[2*], Yanko Todorov[2*], and Donguk Nam[1*]

[1] School of Electrical and Electronic Engineering, Nanyang Technological University, 50 Nanyang Avenue, Singapore 639798, Singapore

[2] Laboratoire de Physique de l'Ecole Normale Supérieure, ENS, Université PSL, CNRS, Sorbonne Université, Université Paris Cité, F-75005 Paris, France

[3] School of Electronic and Electrical Engineering, University of Leeds, Leeds LS2 9JT, UK

[4] School of Electrical Engineering, Korea Advanced Institute of Science and Technology (KAIST), Daejeon 34141, Republic of Korea

[†]These authors contributed equally to this work.

[*]E-mail: dnam@ntu.edu.sg; yanko.todorov@phys.ens.fr; carlo.sirtori@ens.fr

Abstract

Mechanical forces induced by high-speed oscillation provide an elegant way to dynamically alter the fundamental properties of materials such as refractive index, absorption coefficient, and gain dynamics. While the precise control of mechanical oscillation has been well-developed in the past decades, the notion of dynamic mechanical forces has not been harnessed for developing tunable lasers. Here, we demonstrate actively tunable mid-infrared laser action in group-IV nanomechanical oscillators with a compact form factor. A suspended GeSn cantilever nanobeam on a Si substrate is resonantly driven by radio frequency waves. Electrically controlled mechanical oscillation induces elastic strain that periodically varies with time in the GeSn nanobeam, enabling actively tunable lasing emission at >2 μm wavelengths. By utilizing mechanical resonances in the radiowave frequency as a driving mechanism, it might be possible to achieve wide-range mid-infrared tunable lasers with ultra-low power consumption.

Introduction

Actively tunable laser sources are critical for a diverse range of exciting applications such as bio-chemical spectroscopy[1], quantum optics[2], and optical communications[3]. Until now, most of the tunable lasers have relied on thermal tuning mechanisms[3-5], which suffer from limited functionalities such as low tuning efficiency due to their high tuning power consumption. One promising approach to address these limitations is the utilization of microelectromechanical systems (MEMS). By utilizing MEMS-based external cavities, tunable lasers with lower tuning power consumption and higher tuning speed have been reported[6]. Recently, an ultrafast laser frequency tuning was achieved using the electro-optic Pockels effect by integrating a lithium niobate external cavity with III-V gain medium[7,8]. Several other studies have also presented tunable lasers by employing alternative electro-optic effects including the quantum-confined Stark and plasma dispersion effects[9,10]. However, existing demonstrations rely on two disparate systems for a bulky external cavity and gain medium[6,11], preventing the realization of a fully integrated laser device with a compact form factor and also still limiting crucial functionalities such as energy-efficient tuning.

Over the past decade, nanomechanical oscillators with an ultra-small physical volume have been widely exploited for a broad range of applications in the field of nanoelectromechanical systems (NEMS)[12-15]. Particularly, the small physical volume of nanomechanical oscillators allows a very high-frequency mechanical motion, providing versatile platforms for fundamental studies and applications[14]. The mechanical oscillation of nanomechanical oscillators can also be electrically actuated via various means including a dielectric gradient force[12], electrostatic[13], and magnetomotive[15] actuations. This electrically driven motion can enable precise control of mechanical displacement and lattice strain in an oscillating object with a low actuation power[12], thus providing an additional degree of freedom for directly engineering fundamental material properties such as band structure and optical gain.

In this article, we demonstrate electrically tunable mid-infrared laser action in a single integrated GeSn nanomechanical oscillator by actively controlling the mechanical motion. A rapidly oscillating GeSn nanomechanical cantilever combined with an optical cavity emits a single-mode lasing in the mid-infrared spectral range at a cryogenic temperature of 4 K. The active tuning of lasing emission is enabled by applying radio-frequency (RF) drives, which can precisely control the mechanical oscillation, and in turn, the optoelectronic properties of GeSn gain media. Pulsed laser emission can be obtained at any desired moment within a single oscillation period, potentially allowing the experimental investigation of time-resolved mechanical behaviour of rapidly vibrating nanomechanical oscillators. Upon increasing the amplitude of mechanical oscillations, the laser emission wavelength can be actively tuned over a wide range of up to 38 nm with a significantly increased laser intensity due to the modified optical gain spectra, which are supported by rigorous theoretical simulations. Lastly, we show that the use of mechanical resonance allows the emission tuning with low power consumption of 0.24 nW, which is several orders of magnitude smaller than previous demonstrations employing other tuning mechanisms[3,6].

Design of a nanomechanical oscillator for laser tuning

The working principle of the GeSn nanomechanical oscillator with the electrically tunable laser is schematically shown in Fig. 1a. The mechanical oscillation of the nanobeam is controlled by applying an RF drive between the yellow metal electrodes. The resulting non-uniform electric field provides a gradient force[12] on the GeSn nanobeam that simultaneously serves as a mechanical resonator and laser device (Supplementary Note 1). The frequency of the RF drive is matched with the fundamental out-of-plane flexural mode of the nanobeam (3.06 MHz) in order to achieve the maximal amplitude of the mechanical oscillation[12]. The resulting strain in the GeSn gain medium modulates the band structure of GeSn[16], enabling actively tunable laser action.

The layer structure of the device is as follows (Fig. 1a). A step-graded GeSn epilayer with 8-10.6 at% Sn content is grown on a Ge virtual substrate on a Si wafer using low-pressure chemical vapor deposition (LPCVD)[17]. The GeSn-on-insulator (GeSnOI) substrate is produced by using a direct wafer bonding method (Supplementary Note 2)[18]. After bonding, the upper part of the GeSn layer in the original carrier wafer with a Sn content of 10.6 at% is placed at the lower part of the transferred GeSn layer (Supplementary Figure 1). Laser emission originates primarily from the lower part of the GeSn layer with a Sn content of 10.6 at% due to the large optical gain[19]. Also, the smaller energy bandgap in GeSn with a larger Sn content facilitates the funnelling of photoexcited carriers into the lower part of the oscillator[20]. To understand the laser behaviour during the mechanical oscillation, therefore, we only focus on the strain dynamics in the lower part of the oscillator (Supplementary Note 2). The optical fields are confined in an optical cavity between the corner-cube mirror and the end facet of the suspended oscillator. A calculated optical field via 3D finite-difference time-domain (FDTD) simulations reveals strong optical confinement with a *Q*-factor of 480 (Fig. 1b).

Figure 1c presents typical emission spectra from a GeSn nanomechanical oscillator without mechanical actuation. All lasing measurements are conducted at a cryogenic temperature of 4 K (Supplementary Note 3). At a low pump power density, the oscillator produces a broad spontaneous emission with a peak position of 2258 nm, which is consistent with direct bandgap optical transitions from GeSn with a Sn content of 10.6 at%[21]. As the pump power is increased, visible cavity modes appear as a result of the losses being slowly compensated by the material gain, until the system enters the lasing regime with a narrow one-cavity mode at 2266.5 nm. The threshold power density is estimated to be 50.4 kW cm^{-2} (corresponding to 50.4 μJ cm^{-2}) from pump-power dependent photoluminescence (PL) studies (Supplementary Note 4).

Mechanical characterization and simulation

The mechanical oscillation of the GeSn nanobeam is monitored by shining a probe laser onto the device and measuring the intensity fluctuation of the reflected laser beam with a balanced photodetector (Supplementary Note 3). Figure 2a presents the measured photodetector voltage—directly correlated with the amplitude of the mechanical oscillation—as a function of the RF drive frequency at different RF drive amplitude from 1 V to 5 V. A strong peak is observed at an RF drive frequency of 3.062 MHz, which is the fundamental flexural out-of-plane resonance frequency of the GeSn oscillator with a mechanical Q-factor of 1000 (Supplementary Note 5). The absolute amplitude of the mechanical displacement is calibrated by relating the experimental Brownian motion spectrum to the thermal energy in the surrounding environment using the Boltzmann equipartition theorem[22,23] (Supplementary Note 5). Figure 2b shows the calibrated displacement as a function of the applied RF drive featuring a linear dependence with a responsivity of 4.4 nm V^{-1}.

The elastic response of the nanobeam to the RF drive induces a mechanical strain that periodically varies with time, which can be used to directly engineer crucial material properties for achieving active tuning of laser emission. Figure 2c shows the simulated strain distributions under the two maximum displacement conditions for the oscillator driven at the resonance frequency (Supplementary Note 6). The top panel corresponds to the case when the oscillator bends upward, with the compressive strain (blue) and tensile strain (red) above and below the neutral line (black dashed line), respectively. The bottom panel shows the opposite strain distributions when the oscillator bends downward.

Figure 2d shows the simulated time-domain characteristics of the relationship between the RF drive, mechanical displacement, and induced strain (Supplementary Note 5). The top panel presents the RF drive as a function of time t over one period, modelled as $V_{\mathrm{RF}} = V_{\mathrm{p}} \cdot \cos{(\omega_{\mathrm{p}} t)}$, where V_{p} is the peak voltage amplitude, and ω_{p} is the driving frequency set to be resonant with the mechanical eigenmode. The resultant mechanical displacement over time is plotted in the middle panel of Fig. 2d, which has a relative phase shift of −90° with respect to the resonant RF drive. This phase shift stems from the response function of a driven harmonic oscillator (Supplementary Note 5 and Supplementary Fig. 9). The bottom panel of Fig. 2d presents the corresponding average strain induced in the GeSn with 10.6 at% Sn content, lower part of the nanobeam, which is the effective gain region of the laser. The relationship between the RF drive and the strain induced in the oscillator indicates the potential to electrically control the lasing emission in nanomechanical oscillators.

Laser emission characteristics from an actuated oscillator

Figure 3a illustrates the temporal evolution of the laser emission from the oscillator within a single oscillation period. The mechanical displacement (red curve) is actuated by an RF drive with the frequency matched to the mechanical resonance frequency of 3.174 MHz at a cryogenic temperature of 4 K. A pulsed laser with a short pulse width of 1 ns (blue vertical bar) is used to optically pump the oscillator. The frequencies of the pulsed pumping laser and the RF drive are synchronized, while the relative phase $\Delta\Phi$ between the pumping pulse and RF drive is varied to produce laser emission at different moments within one oscillation period (Supplementary Note 3). As shown in the mechanical simulation results (top insets), the gain medium—the lower part of the GeSn layer—experiences different lattice strains depending on the relative phase. For example, the lasing medium is under compressive strain in the first half period (blue shaded area) with a maximum compressive strain at a 90° relative phase while it is under tensile strain in the second half period (red shaded area) with a maximum tensile strain at a 270° relative phase. At relative phases of 0°, 180°, and 360°, the oscillator is not mechanically displaced, and therefore, the lattice strain in the gain medium should be negligible.

Figure 3b presents laser spectra of the device measured at different relative phases from 0° to 360° with a step of 30°. The amplitude of the RF drive is fixed to 10 V. Figure 3c shows the peak wavelengths (top), intensities (bottom), and full-width at half-maximum (FWHM) (bottom inset) of the emission spectra as a function of the relative phase. At a 0° relative phase, the laser peak is observed at 2266.5 nm (Peak 1), which is the same as the one measured without the RF drive (Fig. 1c). When the relative phase is changed from 0° to 360°, it is clearly shown that the lasing peak wavelength and intensity vary periodically, which is in phase with the mechanical displacement (Fig. 3a). When the relative phase is varied from 0° to 90°, the emission wavelength is continuously blue-shifted due to the compressive strain in the gain medium. It should be noted that we define such continuous and fine emission wavelength shifts as fine tuning. The mechanism for the fine tuning will be explained in Fig. 4a. This emission intensity is also reduced while the FWHM is increased. Note that the influence of the mechanical displacement of the oscillator on the laser emission intensity is negligible (Supplementary Note 7). When the relative phase is changed from 90° to 180°, all three lasing parameters—the emission wavelength, intensity, and FWHM—gradually return to the values measured at a 0° relative phase, indicating that the mechanical state of the oscillator is restored to the original condition with no displacement, as illustrated in Fig. 3a. The observed FWHM broadening and narrowing are proportional to the inverse of the output laser power, which is consistent with the Schawlow–Townes equations. Surprisingly, when the relative phase is increased from 180° to 210°, a new strong laser mode (Peak 2) emerges at 2303.7 nm while the original mode (Peak 1) quenches. This new peak is at 37.2 nm away from the original peak, which cannot be explained simply by considering a continuous variation of material properties such as refractive index, as strain is gradually changed. The observed switching of the laser mode is defined as coarse tuning, which is a widely accepted terminology for thermal heater-based tunable lasers[3]. The mechanism for the coarse tuning will be explained in detail in Figs. 4b and c. This new peak also varies periodically as a function of the relative phase. As the relative phase is changed from 330° to 360°, the laser parameters return to the values measured in the absence of mechanical displacement. This periodical dependence of laser characteristics on the relative phase reveals a direct correlation between the mechanical motion (Fig. 3a) and laser emission (Fig. 3c). For example, the relative phases for no mechanical displacement can be experimentally verified to be 0°, 180°, and 360°, while the largest (smallest) values for the wavelength and intensity at 270° (90°) confirms the maximum displacement point with tensile (compressive) strain. It should be noted that the lasing emission wavelength can be continuously shifted and actively controlled simply by adjusting the RF drive amplitude (Supplementary Note 8). The coarse-tuning range of 37.6 nm (equivalent to ~2.2 THz) with the fine-tuning range of 1 nm (equivalent to ~50 GHz) is obtained with a relatively small RF drive of 10 V.

Theoretical analysis for the laser tuning behaviour

Comprehensive theoretical analyses are performed to understand the mechanisms for two distinct tuning schemes: fine tuning and coarse tuning. The mechanism for the fine tuning can be understood by considering the strain-induced refractive index change. Figure 4a shows the calculated refractive index change Δn in GeSn as a function of the relative phase by using the Lorentz-Lorenz equation[24]. This periodical behaviour of Δn is consistent with the observed continuous spectral shift of Peak 1 (blue shade) and Peak 2 (red shade) in the top panel of Fig. 3c. Therefore, this fine shift in wavelength can be attributed to the strain-induced refractive index modulation in the GeSn gain medium, which leads to a change in the effective optical length and subsequently results in emission wavelength shift. It should be noted that the RF drive-induced capacitive effect that can modify the refractive index via charge accumulations is confirmed to be negligible for the emission wavelength tuning (Supplementary Note 9).

To investigate the mechanism for coarse tuning, we first calculate the material gain spectra of GeSn with a Sn content of 10.6 at% under different mechanical strains (Fig. 4b) by using the 8-band $\mathbf{k}\cdot\mathbf{p}$ model and numerical analyses (Supplementary Note 10). At 0% strain (blue curve), the maximum material gain is observed at 2259.4 nm. At a tensile strain of 0.1% (red curve), the peak position of the material gain is shifted by 39.9 nm to a longer wavelength of 2299.3 nm, while the gain magnitude is increased. The changes in the peak position and magnitude can be attributed to the bandgap shrinkage and improved directness under tensile strain, respectively[16]. At a compressive strain of –0.1% (black curve), the gain spectrum is changed oppositely to the tensile strain case.

Figure 4c presents a simulated optical spectrum of our cavity design. The mechanism for the coarse tuning can be understood from Figs. 4b and c. At a 180° relative phase, the oscillator is not under mechanical strain and the gain peak is at 2259.4 nm, near the simulated Peak 1 in Fig. 4c. When the relative phase is changed to 210° or larger values, the oscillator starts experiencing tensile strain in the lasing medium. As the gain peak position is shifted to a longer wavelength under tensile strain, the peak gain wavelength is shifted closer to the simulated Peak 2 in Fig. 4c, resulting in the sudden emergence of Peak 2 in Fig. 3b. The calculated material gain shift (39.9 nm) and wavelength difference between the simulated Peak 1 and Peak 2 (37 nm) are in excellent agreement with the experimentally observed lasing peak shift of 37.2 nm. On the other hand, the maximum compressive strain of –0.1% at the relative phase between 0° and 180° shifts the gain peak position only by –19.4 nm, which is insufficient to change the dominant lasing mode to a shorter wavelength.

Conclusions

In summary, we have shown an actively tunable laser integrated in a single GeSn nanomechanical oscillator with a compact form factor. Our device harnesses mechanical resonances actuated by an RF drive to dynamically control the strain in the laser gain medium for laser emission tuning. This tuning scheme achieves emission tuning at orders-of-magnitude lower power consumption than other tuning schemes, such as thermal heater[3,25,26], MEMS cavity[6,27], electro-optic based devices[9,10] (Supplementary Table 1). Lasing wavelength tuning consumes just 0.24 nW for tuning 37.6 nm (equivalent to ~2.2 THz) (Supplementary Note 11). This leads to a tuning efficiency of 156.7 nm/nW (equivalent to ~9.17 THz/nW), which is several orders of magnitude higher than thermal heater-, MEMS cavity-, and electro-optic-based tunable lasers. This improved tuning efficiency stems from the use of resonant oscillation in nanomechanical oscillator with a high mechanical Q-factor, which can enhance the mechanical responsivity in response to the applied RF drive by several orders of magnitude compared to the static mechanical response. It is also possible to further increase the tuning efficiency by improving the mechanical Q-factor[28].

The lasing characteristics that are varied periodically by the rapid mechanical oscillatory motion allow monitoring the mechanical state of the oscillator in real time. Strong coupling between mechanical modes and amplified optical fields in the integrated gain media may enable the realization of an innovative class of devices to study light-matter interaction in active optomechanics cavities[29,30]. Also, the direct observation of time-varying material properties in the oscillator can provide insights into building a time crystal, which requires the state of an object to be modulated periodically in time[31]. While the oscillation frequency of the current device is at the MHz range, it should be possible to increase the oscillation frequency beyond the GHz range by optimizing the geometry of the oscillator[32] for enabling a high-frequency nanomechanical time crystal and high-speed optical communication (Supplementary Note 12). Our demonstration of a direct coupling between lasing emission and mechanical motion offers a practical solution for ultra-small and low-power mid-infrared tunable lasers integrated on Si while providing possibilities of nanomechanical concepts for a broad range of optoelectronics applications.

Acknowledgements

This work is supported by National Research Foundation of Singapore through the NRF-ANR Joint Grant (NRF2018-NRF-ANR009 TIGER). This work is also supported by National Research Foundation of Singapore through the Competitive Research Program (NRF-CRP19-2017-01). This work is also supported by the iGrant of Singapore A*STAR AME IRG

(A2083c0053). This research is also supported by the National Research Foundation, Singapore and A*STAR under its Quantum Engineering Programme (NRF2022-QEP2-02-P13). The authors would like to acknowledge and thank the Nanyang NanoFabrication Centre (N2FC). The authors also thank Dr. Di Zhu, Dr. Jeremy Witzens, and Dr. Bahareh Marzban for the fruitful discussions.

Author contributions

D.N., C.S., and Y.T. conceived the initial idea of the project. H.-J.J. fabricated the samples. H.-J.J. and D.N. planned the optical experiments. H.-J.J. and M.C. carried out optical measurements. J.L. and B.C. conducted mechanical characterization measurements. A.V. and D.G. assisted with the mechanical measurement setup. Under the guidance of D.N., Y.T., and C.S., H.-J.J. and J.L. performed data analysis. Y.K. optimized the laser structure by performing optical simulations. Z.I. conducted the band structure simulations and gain modelling. K.L. and X.S. assisted with the optical measurement setup. Y.-I.S. contributed to the RF drive setup construction. L.Z. and C.S.T. prepared the GeSn wafer. D.B. fabricated the GeSnOI substrates. H.-J.J. and D.N. led the manuscript writing with input from J.L., M.C., D.B., C.S., and Y.T. All authors discussed the data and participated in preparing the manuscript.

Competing interests

The authors declare no competing interests.

Figure legends

Fig. 1 | Design of a GeSn nanomechanical oscillator for actively tunable laser action. a, Schematic illustration of an actively tunable laser consisting of a nanomechanical GeSn oscillator integrated with corner-cube and end facet mirrors for an optical cavity. The GeSn oscillator is actuated by an RF drive applied on the metal electrodes, inducing periodically varying lattice strain in the lasing medium over time. The lasing medium is photo-excited with a 1550-nm pulsed laser. Top inset: cross-sectional transmission electron microscopy image of the GeSnOI substrate. Scale bar, 400 nm. Bottom inset: tilted-view scanning electron microscopy image of the fabricated GeSn nanomechanical oscillator. Scale bar, 5 µm. **b,** Top: top-view SEM image. Scale bar, 10 µm. Bottom: simulated optical field distribution in the GeSn oscillator. Strong optical confinement between the corner-cube mirror and the end facet of the oscillator is observed in the cavity. **c,** Evolution of emission spectra from the GeSn oscillator measured without mechanical actuation. A clear transition from a broad spontaneous emission to single-mode lasing is observed by increasing the pump power density. The emission intensity of the bottom and middle spectra are multiplied by a factor of 1200 and 600, respectively.

Fig. 2 | Mechanical characterization and simulation. a, Mechanical responses of the oscillator actuated by RF drive with different amplitudes from 1 V to 5 V. The mechanical resonance is at 3.062 MHz and the FWHM is about 3 kHz. The measurements are conducted at 300 K in a low-pressure environment of 1 mbar. **b,** Calibrated displacement of the oscillating cantilever (blue circles) as a function of the RF drive measured in panel **a**. The displacement has a linear dependence with the amplitude of RF drive, with a responsivity of 4.4 nm V^{-1} as fitted by the dashed blue line. **c,** 3D finite element method simulations of strain distributions in the GeSn oscillator with different bending directions (deformation is exaggerated for better visualization). Panels below the tilted 3D views depict the corresponding strain distribution in the x-z cross-section. Blue (red) colour indicates compressive (tensile) strain. Black dashed lines in the cross-sectional views indicate the neutral line in the strained beam. **d,** Time-domain characteristics showing RF drive (top), mechanical displacement (middle), and induced strain (bottom).

Fig. 3 | Laser emission characteristics from an actuated oscillator. a, PL measurement scheme. Top insets show mechanical simulation results under different bending motions. The GeSn gain medium is pumped with a pulsed laser with a short pulse width of 1 ns (blue vertical bar) that is significantly shorter than the oscillation period, enabling the observation of lasing emission from the oscillator under specific bending motions. **b,** Lasing spectra from the device at different relative phases $\Delta\Phi$ from 0° to 360° with a 30°/step at a fixed RF drive V_{RF} of 10 V. Inset: magnified view of lasing spectra for Peak 1 and Peak 2 measured at relative phases from 90° to 270° with the same step of 30°. **c,** Corresponding emission wavelength (top), intensity (bottom), and FWHM (inset) of Peak 1 and Peak 2 as a function of the relative phase are plotted by using a Lorentzian fitting to the experimental data.

Fig. 4 | Theoretical analysis for the laser tuning behaviour. a, Calculated refractive index change Δn as a function of the relative phase in a vibrating GeSn oscillator. **b,** Calculated material gain for GeSn with a Sn content of 10.6 at% under various uniaxial strains. **c,** Simulated optical spectrum of the cavity design used in this study.

References

1. Choi, J.-H. *et al.* A high-resolution strain-gauge nanolaser. *Nature Communications* **7**, 11569 (2016).
2. Niffenegger, R. J. *et al.* Integrated multi-wavelength control of an ion qubit. *Nature* **586**, 538-542 (2020).
3. Corato-Zanarella, M. *et al.* Widely tunable and narrow-linewidth chip-scale lasers from near-ultraviolet to near-infrared wavelengths. *Nature Photonics* **17**, 157-164 (2023).
4. Shim, E. *et al.* Tunable single-mode chip-scale mid-infrared laser. *Communications Physics* **4**, 268 (2021).
5. Xin, M. *et al.* Optical frequency synthesizer with an integrated erbium tunable laser. *Light: Science & Applications* **8**, 122 (2019).

6. Huang, M. C. Y., Zhou, Y. & Chang-Hasnain, C. J. A nanoelectromechanical tunable laser. *Nature Photonics* **2**, 180-184 (2008).
7. Snigirev, V. *et al.* Ultrafast tunable lasers using lithium niobate integrated photonics. *Nature* **615**, 411-417 (2023).
8. Li, M. *et al.* Integrated Pockels laser. *Nature Communications* **13**, 5344 (2022).
9. Ueda, Y., Shindo, T., Kanazawa, S., Fujiwara, N. & Ishikawa, M. Electro-optically tunable laser with ultra-low tuning power dissipation and nanosecond-order wavelength switching for coherent networks. *Optica* **7**, 1003-1006 (2020).
10. Andreou, S., Williams, K. A. & Bente, E. A. J. M. Electro-Optic Tuning of a Monolithically Integrated Widely Tuneable InP Laser With Free-Running and Stabilized Operation. *Journal of Lightwave Technology* **38**, 1887-1894 (2020).
11. Huang, M. C. Y., Zhou, Y. & Chang-Hasnain, C. J. A surface-emitting laser incorporating a high-index-contrast subwavelength grating. *Nature Photonics* **1**, 119-122 (2007).
12. Unterreithmeier, Q. P., Weig, E. M. & Kotthaus, J. P. Universal transduction scheme for nanomechanical systems based on dielectric forces. *Nature* **458**, 1001-1004 (2009).
13. Liu, N. *et al.* Time-domain control of ultrahigh-frequency nanomechanical systems. *Nature Nanotechnology* **3**, 715-719 (2008).
14. Li, M., Tang, H. X. & Roukes, M. L. Ultra-sensitive NEMS-based cantilevers for sensing, scanned probe and very high-frequency applications. *Nature Nanotechnology* **2**, 114-120 (2007).
15. Henry Huang, X. M., Zorman, C. A., Mehregany, M. & Roukes, M. L. Nanodevice motion at microwave frequencies. *Nature* **421**, 496-496 (2003).
16. Gupta, S., Magyari-Köpe, B., Nishi, Y. & Saraswat, K. C. Achieving direct band gap in germanium through integration of Sn alloying and external strain. *Journal of Applied Physics* **113**, 073707 (2013).
17. Burt, D. *et al.* Direct bandgap GeSn nanowires enabled with ultrahigh tension from harnessing intrinsic compressive strain. *Applied Physics Letters* **120**, 202103 (2022).
18. Burt, D. *et al.* Strain-relaxed GeSn-on-insulator (GeSnOI) microdisks. *Opt. Express* **29**, 28959-28967 (2021).
19. Dutt, B. *et al.* Theoretical analysis of GeSn alloys as a gain medium for a Si-compatible Laser. *IEEE Journal of Selected Topics in Quantum Electronics* **19**, 1502706-1502706 (2013).
20. Nam, D. *et al.* Strain-Induced Pseudoheterostructure Nanowires Confining Carriers at Room Temperature with Nanoscale-Tunable Band Profiles. *Nano Letters* **13**, 3118-3123 (2013).
21. Joo, H.-J. *et al.* 1D photonic crystal direct bandgap GeSn-on-insulator laser. *Applied Physics Letters* **119**, 201101 (2021).
22. Cleland, A. N. & Roukes, M. L. Noise processes in nanomechanical resonators. *Journal of Applied Physics* **92**, 2758-2769 (2002).
23. Liu, J. *et al.* Ultrafast detection of terahertz radiation with miniaturized optomechanical resonator driven by dielectric driving force. *ACS Photonics* **9**, 1541-1546 (2022).
24. Tran, H. *et al.* Systematic study of Ge1−xSnx absorption coefficient and refractive index for the device applications of Si-based optoelectronics. *Journal of Applied Physics* **119**, 103106 (2016).
25. Brian Sia, J. X. *et al.* Sub-kHz linewidth, hybrid III-V/silicon wavelength-tunable laser diode operating at the application-rich 1647-1690 nm. *Opt. Express* **28**, 25215-25224 (2020).

26. Chu, T., Fujioka, N. & Ishizaka, M. Compact, lower-power-consumption wavelength tunable laser fabricated with silicon photonic wire waveguide micro-ring resonators. *Opt. Express* **17**, 14063-14068 (2009).
27. Huang, M. C. Y., Zhou, Y. & Chang-Hasnain, C. J. Nano electro-mechanical optoelectronic tunable VCSEL. *Opt. Express* **15**, 1222-1227 (2007).
28. Beccari, A. *et al.* Strained crystalline nanomechanical resonators with quality factors above 10 billion. *Nature Physics* **18**, 436-441 (2022).
29. Yu, D. & Vollmer, F. Active optomechanics. *Communications Physics* **5**, 61 (2022).
30. Czerniuk, T. *et al.* Lasing from active optomechanical resonators. *Nature Communications* **5**, 4038 (2014).
31. Lyubarov, M. *et al.* Amplified emission and lasing in photonic time crystals. *Science* **377**, 425-428 (2022).
32. Gaidarzhy, A., Zolfagharkhani, G., Badzey, R. L. & Mohanty, P. Spectral response of a gigahertz-range nanomechanical oscillator. *Applied Physics Letters* **86**, 254103 (2005).

Data Availability

The data that support the findings of this study are available within the main text and Supplementary Information. Any other relevant data are available from the corresponding authors upon request.

Additional information

Supplementary information is available in the online version of the paper. Correspondence and requests for materials should be addressed to D.N., Y. T., and C.S.

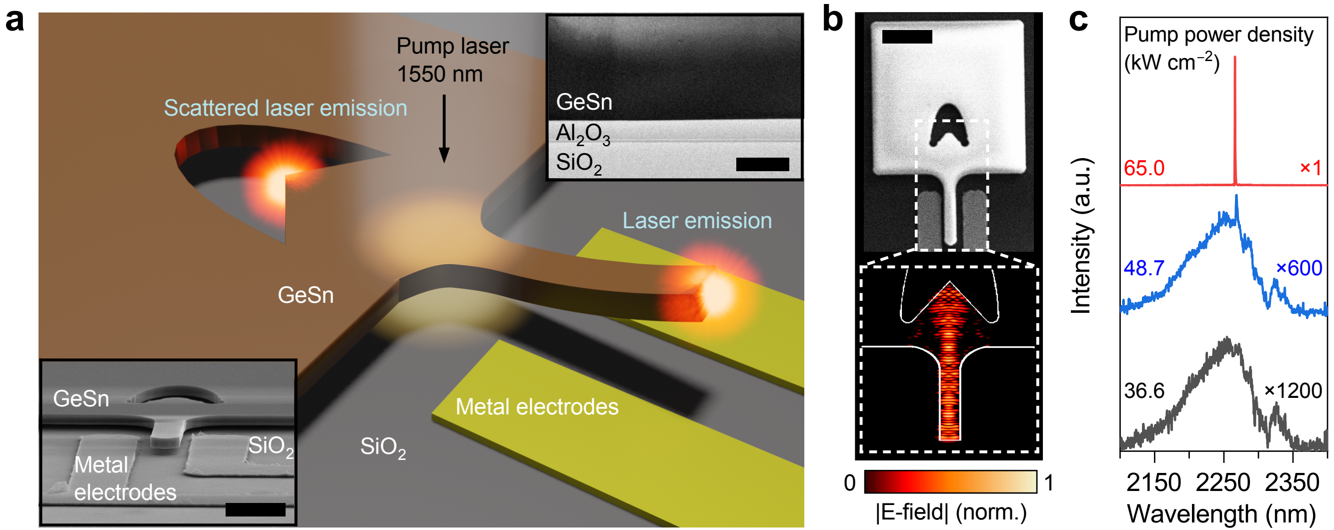
a
Pump laser
1550 nm
Scattered laser emission
GeSn
Al2O3
SiO2
Laser emission
GeSn
GeSn
Metal electrodes
SiO2
SiO2
Metal
electrodes
b
0
1
|E-field| (norm.)
c
Pump power density
(kW cm−2)
65.0
×1
48.7
×600
36.6
×1200
Intensity (a.u.)
2150
2250
2350
Wavelength (nm)

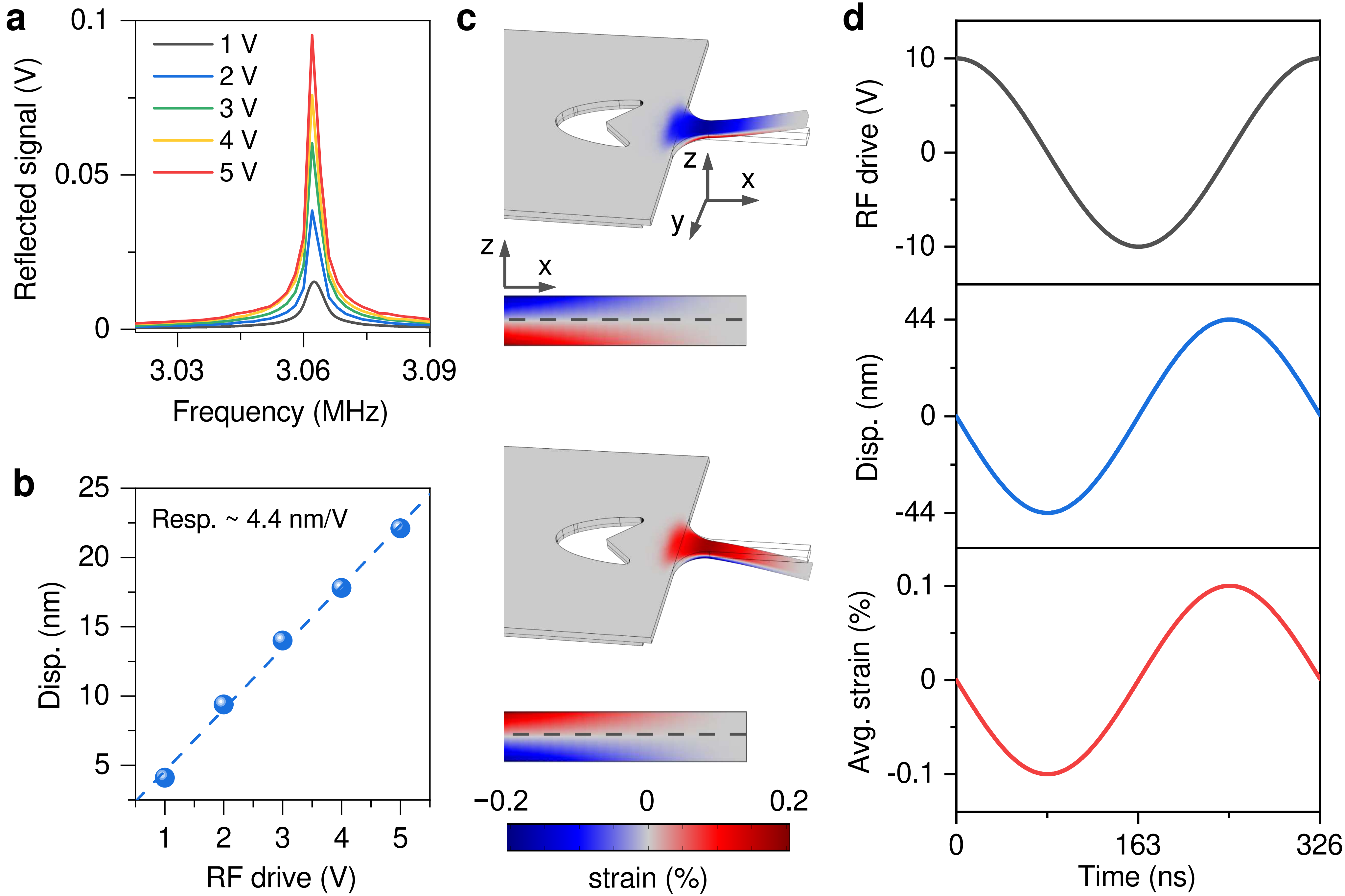

a
0.1
0.05
0
1 V
2 V
3 V
4 V
5 V
Reflected signal (V)
3.03
3.06
3.09
Frequency (MHz)
b
Resp. ~ 4.4 nm/V
25
20
15
10
5
Disp. (nm)
1
2
3
4
5
RF drive (V)
c
z
x
y
z
x
−0.2
0
0.2
strain (%)
d
10
0
-10
RF drive (V)
44
0
-44
Disp. (nm)
0.1
0
-0.1
Avg. strain (%)
0
163
326
Time (ns)

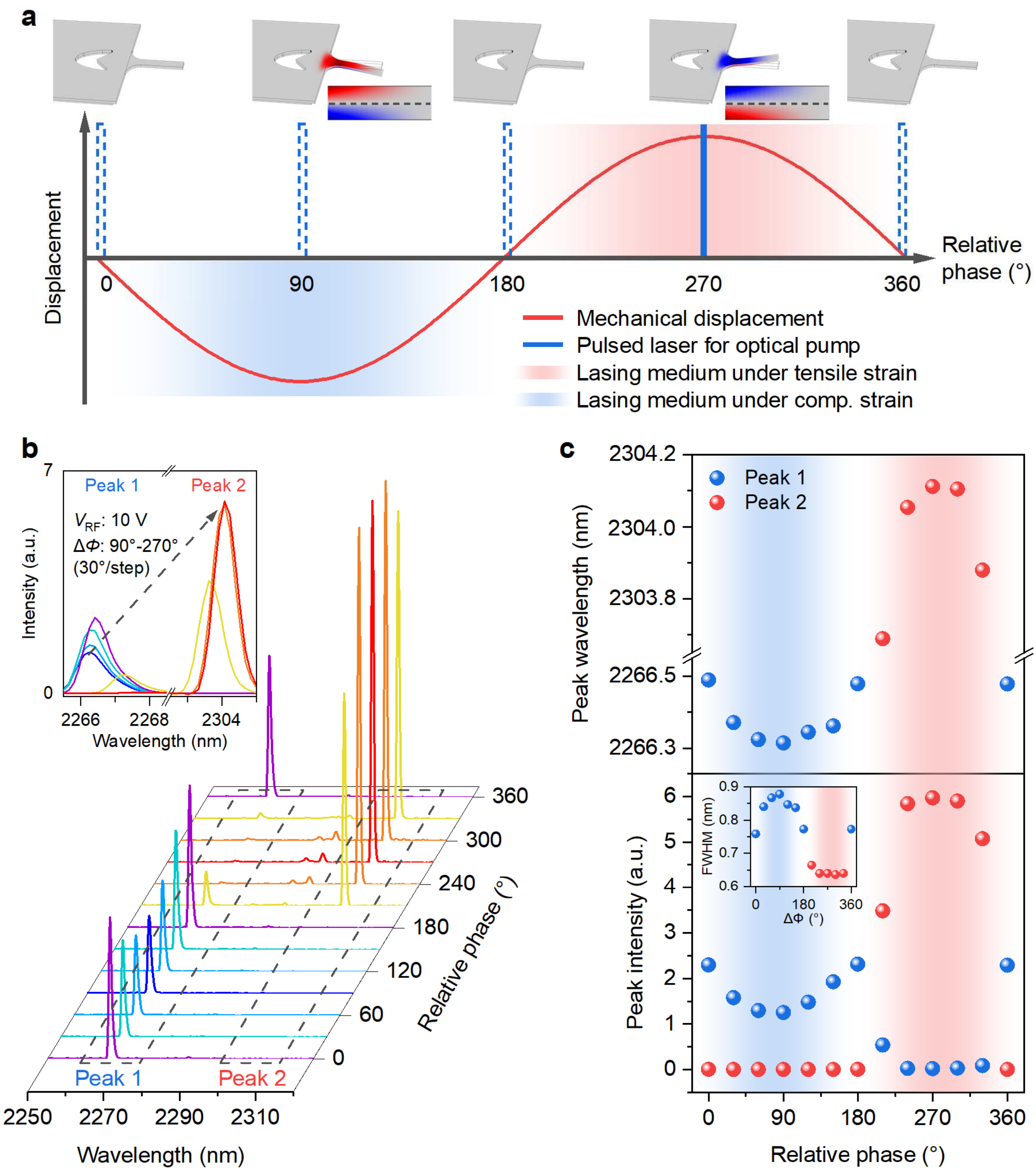

a
Displacement
0
90
180
270
360
Relative phase (°)
Mechanical displacement
Pulsed laser for optical pump
Lasing medium under tensile strain
Lasing medium under comp. strain
b
Peak 1
Peak 2
V_{RF}: 10 V
$\Delta\Phi$: 90°-270°
(30°/step)
Intensity (a.u.)
7
0
2266
2268
2304
Wavelength (nm)
360
300
240
180
120
60
0
Relative phase (°)
2250
2270
2290
2310
Wavelength (nm)
c
Peak 1
Peak 2
Peak wavelength (nm)
2304.2
2304.0
2303.8
2266.5
2266.3
Peak intensity (a.u.)
6
5
4
3
2
1
0
FWHM (nm)
0.9
0.8
0.7
0.6
0
180
360
ΔΦ (°)
0
90
180
270
360
Relative phase (°)

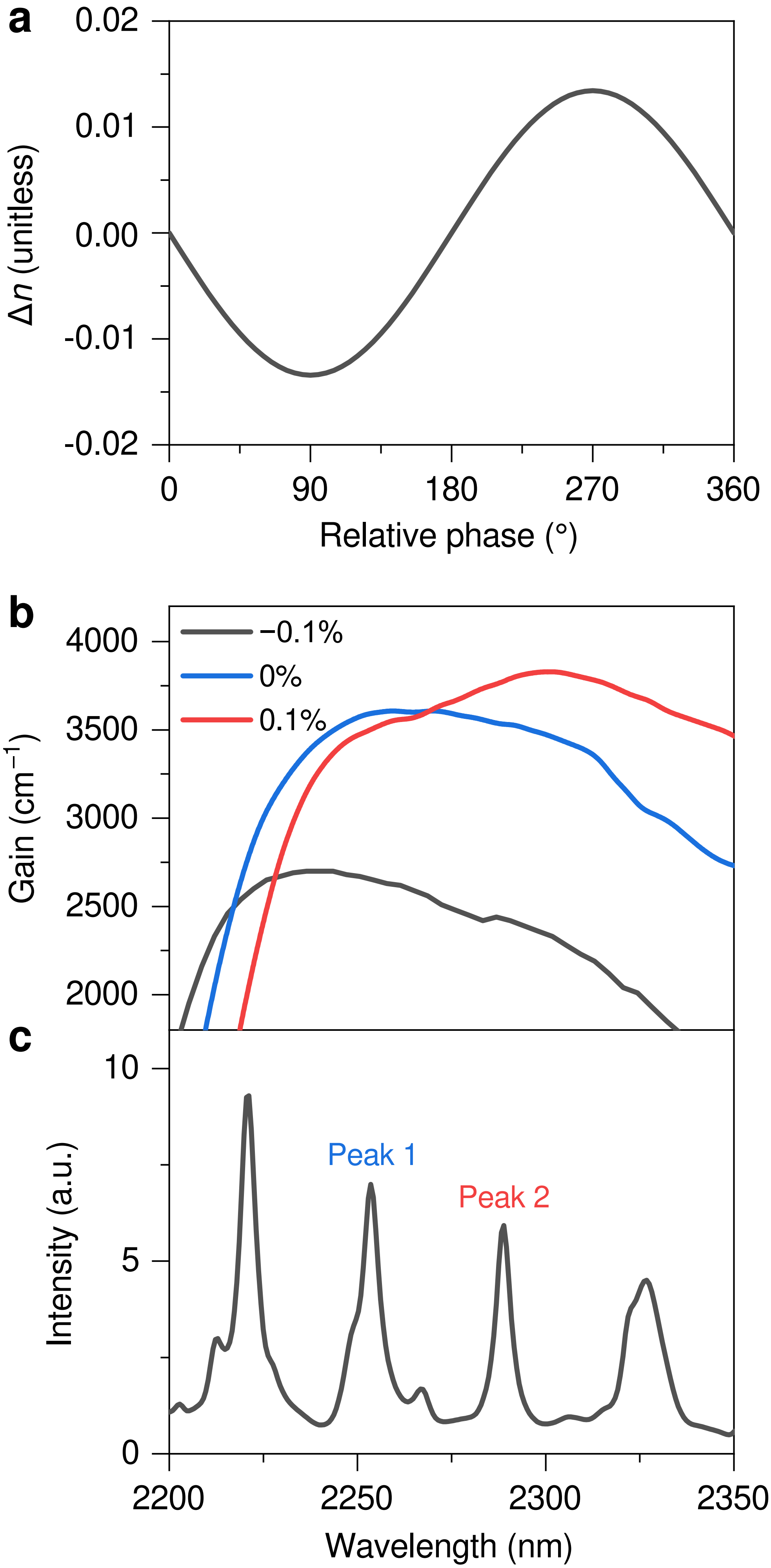
a
Δn (unitless)
0.02
0.01
0.00
-0.01
-0.02
0
90
180
270
360
Relative phase (°)
b
−0.1%
0%
0.1%
Gain (cm⁻¹)
4000
3500
3000
2500
2000
c
Intensity (a.u.)
10
5
0
Peak 1
Peak 2
2200
2250
2300
2350
Wavelength (nm)

Table of Content

Note 1. Gradient force

The force considered here is related to a fundamental property of any dielectric material: its polarizability. When a small dielectric body is placed in an inhomogeneous electric field, it is polarized, and a net dipole appears in the direction of the field. The body is then driven towards to the high electric field region, resulting in a net force. Such forces appear for any material that has a linear susceptibility, and in that sense, they are universal[1]. It is worth noting that this gradient force-based driving scheme has been successfully employed for various semiconductor and dielectric materials[1-3].

Note 2. Sample preparation

The GeSn layer was grown on a Ge virtual substrate on a 6-inch Si wafer by low-pressure chemical vapor deposition (LPCVD). The Sn content in the GeSn layer varies from ~8 at% to ~10.6 at%. At the bottom part of the GeSn layer, the Sn content is ~8 at%. As the thickness increases, the compressive strain relaxes at a critical thickness (~200 nm), allowing more Sn atoms to be introduced into the lattice. This results in a compositional Sn gradient, for a thickness of ~400-nm. Finally, the strain cannot relax any further and remains constant, resulting in a top layer with a Sn content of 10.6 at% and a thickness of ~300 nm[4]. Supplementary Figure 1a shows a cross-sectional schematic of the material stack for an as-grown sample. The transmission electron microscope (TEM) image is shown in the inset of Supplementary Fig. 1a, showing the defective GeSn/Ge and Ge/Si interfaces[5], which occur because of the significant lattice mismatches in the system. Supplementary Figure 1b shows a cross-sectional schematic of the final GeSnOI material stack used in this study, while the inset shows the same TEM image presented in Fig. 1a in the main text. The fabricated GeSnOI substrate consists of a GeSn layer with a Sn content of 8 at% at the upper part and 10.6 at% at the lower part. It is worth mentioning that the lower part of the GeSn layer (10.6 at%) has a smaller material bandgap compared to that of the upper part (8 at%) due to the higher Sn composition[6]. When the GeSn layer is subjected to optical excitation, photoexcited carriers are funnelled into the lower part with a smaller bandgap[7]. Even when the oscillator bends downward inducing tensile (compressive) strain in the upper (lower) part of the oscillator, the lower part still has a smaller bandgap than the upper part, serving as a gain medium.

To provide further insight into the bandgap of the compositionally graded GeSn layer, we conducted band structure calculations using the 8-band k·p method. In Supplementary Fig 2a, we present the calculated bandgap energies of the GeSn layers with 8 at% and 10.6 at% as a function of uniaxial strain at 4 K. It is evident that the 10.6 at% GeSn under the compressive strain of –0.1% (red circle) retains a much smaller bandgap compared to 8 at% GeSn under the tensile strain of 0.1% (blue square). This is because the Sn content difference of 2.6 at% contributes to the bandgap reduction much more significantly than the strain difference between –0.1% compressive and 0.1% tensile strains[6].

It should be noted that the alignment of band edges within the GeSn layers plays a crucial role in determining the gain medium of the laser. To investigate the band edge alignment of our compositionally graded GeSn layer, we calculated the band diagram along the sample depth direction, as depicted in Supplementary Fig. 2b. Our analysis considered the conduction band (E_c) and valence band (E_v) edges of the bandgap. In the upper part of the GeSn layer from 0 nm to ~500 nm, the increasing Sn content along the depth direction reduces the bandgap, leading to a tilted band edge. Such a tilted band edge is widely exploited in many semiconductor lasers employing graded heterostructures to improve the laser threshold by confining the carriers in the smaller bandgap region[7-10]. On the other hand, in the lower part of the GeSn layer from ~500 nm to 800 nm, the uniform Sn content leads to unaltered band edges. The tilted band edge in the upper part induces a carrier funneling effect, causing photoexcited carriers in the GeSn layer to funnel from the large bandgap (upper part) to the small bandgap (lower part). This results in carrier accumulation in the lower part of the GeSn layer, allowing the lower part of the GeSn layer to serve as a gain medium.

To produce the GeSnOI sample, a direct wafer bonding process was adopted as schematically shown in Supplementary Fig. 3a. A Si handle wafer with a 1000-nm thick silicon dioxide (SiO_2) layer was prepared. Both the Si handle wafer and the carrier wafer with an epitaxial GeSn layer were diced into 3 cm^2 chips. These chips were cleaned using acetone and isopropanol, followed by the deposition of a 200-nm thick Al_2O_3 layer using atomic layer deposition (ALD). Furnace annealing was performed at 250 ºC to outgas any residual gas in the layers. Chemical mechanical polishing (CMP) was used to achieve a smooth surface for bonding, which is required to obtain a high bond strength. Then, the two surfaces of the handle and carrier chips were made to contact for a pre-bonding. Annealing at 250 ºC was performed in an inert ambient condition with N_2. The top Si layer in the carrier chip was etched by a combination of mechanical polishing and wet etching using potassium hydroxide (KOH). A final CMP step was used to remove the Ge buffer layer (including the defective interfaces), resulting in the final GeSnOI with a high-quality GeSn layer with minimized defects.

Supplementary Figure 3b shows the schematic fabrication flow for the GeSn oscillators. The photoresist AZ5214E was spin-coated at 6000 rpm for 90 seconds to produce a thickness of 1100-nm, followed by a hot plate bake for 90 seconds at 110 ºC. Photolithography with ultraviolet (UV) radiation was then used to define GeSn cantilever structures and corner cube mirrors. Anisotropic reactive ion etching (RIE) using chlorine-based gases was used to pattern the GeSn layer. Wet etching using hydrofluoric (HF) acid was then employed to undercut and suspend the cantilever structure by removing all the Al_2O_3 layer and a part of the SiO_2 layer under the patterned GeSn cantilever structure. A harmful residual compressive strain in the GeSn layer was relaxed during the wet etching process[11]. A second photolithography step was used to produce metal contacts on the remaining SiO_2 layer, which were used to apply the radio-frequency (RF) drive. Deposition of the metal electrodes was achieved by using electron beam evaporation (EBE) with a 20-nm chromium and 180-nm gold layers, followed by a solvent-based lift-off process.

Raman spectroscopy was used to verify that the residual compressive strain in the suspended cantilever had relaxed. We used a ×100 objective lens to focus a 532-nm pump laser onto the GeSn cantilevers with a spot diameter of ~1 um. The experimentally obtained Raman spectra of the fabricated devices at the cantilever center are displayed in Supplementary Fig 4. We observed a 1.8 cm^{-1} Raman peak shift between the unrelaxed (294.2 cm^{-1}) and relaxed (292.4 cm^{-1}) GeSn cantilever. Using a Raman-strain shift coefficient[12] of 521 cm^{-1}, the associated residual compressive strain of the GeSn layer was calculated to be ~0.35%.

Note 3. Experimental setups

Photoluminescence (PL) measurements: Supplementary Figure 5a shows a schematic of the PL measurement setup. Firstly, the samples are mounted inside a helium cryostat, which can function between 4 and 300 K. A free space 1550-nm pulsed laser (CoLID-I-1550, Connet Laser Technology) with a pulse width of 1 ns is used to produce the input pump. The pump laser was coupled into a ×15 reflective objective which was used for two functions: (1) it focuses the pump laser onto the center of the cantilever and (2) it collects the generated output signal from the cantilever. The measured output signal is reflected by the half mirror and coupled into a Fourier transform infrared (FTIR) spectrometer with a spectral resolution of ~0.15 nm. Finally, the output signal passes through a long-pass filter (LPF) to remove the pump laser signal before entering an extended InGaAs (IGA) detector to produce the spectrum. During the relative phase $\Delta\Phi$ and RF drive V_{RF} dependence measurements, the device is optically pumped at 4 K by a 1550-nm pulsed laser at a fixed pump power of 56.9 kW cm^{-2}. To synchronize the pump laser to the RF drive, the pump laser was phase-locked to the RF drive while both frequencies of pump laser and RF drive were fixed at mechanical resonant frequency of 3.174 MHz. A tunable RF phase delay was used to control the RF phase relative to the pump laser.

Mechanical measurements: The device is inserted in a vacuum chamber (~1 mbar) at room temperature for the micro-mechanical characterizations. Supplementary Figure 5b presents the homebuilt optical microscope to measure the mechanical oscillation of a single device. A microscope objective (N.A. = 0.5) is employed to focus the near-infrared probe laser (λ = 930 nm) onto the device under test with a spot size on the order of 1 μm in diameter. This laser beam will be modulated and reflected by the oscillating cantilever, which is then collected by the same objective, split into two paths by a D-shape edge, and recorded by a balanced photodiode (Thorlabs PDB110A). This optical probing method is very sensitive and allows exceptional signal to noise ratio. Therefore, the Brownian motion peak induced by the thermal noise in the environment can be well-resolved in the mechanical RF spectrum, which is critical for the mechanical calibration as shown later in Supplementary Note 5. A spectral analyser (Agilent CXA N9000A) is used to visualize the Brownian motion mode of the nanomechanical device and its mechanical responses to RF drive.

Note 4. Laser characteristics

Supplementary Figure 6a shows light-in light-out (L-L) characteristics of GeSn cantilever under 1550-nm pulsed laser excitation in the absence of RF drive. The measurement was carried out at 4 K. The observation of clear threshold behaviour in the L-L curve provides unequivocal evidence of lasing action. Using a linear fit, we obtained a threshold power density of 50.4 kW cm^{-2} (corresponding to 50.4 μJ cm^{-2}). It should be noted that the threshold value of our device is comparable with other GeSn-based group IV lasers[13-15]. The threshold power density can be improved via several approaches such as improving the bandgap directness of the GeSn gain medium and optimizing the optical cavity design. The bandgap directness of GeSn can be improved by introducing a static tensile strain in the GeSn gain medium using external stressor layers[16]. Optimizing the cavity design, such as employing photonic crystal cavities, may also reduce the lasing threshold by reducing optical losses. Additionally, the double-logarithmic plot in the inset exhibits typical S-shaped emission. Supplementary Figure 6b presents the full-width at half-maximum (FWHM) of the lasing peak as a function of pump power density. A reduction in the FWHM from ~2.21 nm to ~ 0.65 nm was observed which provides additional evidence of lasing.

Note 5. Mechanical measurements and analyses

To investigate the mechanical eigenmode of the device, the mechanical experiments are conducted by directly measuring the Brownian motion peak induced by the thermal noise in the surrounding environment. Supplementary Figure 7a presents the experimental Brownian motion peak (blue dots) of the device, which can be well fitted by the red curve, i.e., a sum of a Lorentzian distribution (blue line) and a noise floor (black dashed line). This peak is measured at 3.062 MHz with a quality factor of ~1000, corresponding to the fundamental out-of-plane flexural vibration mode of the beam. This Brownian motion peak can be exploited for calibration of the mechanical response[3,17]. By relating its power density spectrum to the thermal energy $k_B T$ (where k_B is the Boltzmann constant and T is the temperature), one can convert the measured signal from voltage power spectral density S_{vv} (V^2/Hz) to the motion power spectral density S_{zz} ($\mathrm{pm}^2/\mathrm{Hz}$) as shown in Supplementary Fig. 7a, from which the displacement of the mechanical beam is accessible. The fundamental out-of-plane flexural vibration mode of the beam is visualized by the finite element method (FEM) in Supplementary Fig. 7b.

To explore the mechanical response to the periodic external drive, the RF drive applied to the metal electrodes is modulated using a function generator and the resultant driving voltage is in the form of $V_{\mathrm{RF}} = V_{\mathrm{p}} \cdot \cos(\omega_{\mathrm{p}} t)$, where V_{p} is the peak voltage amplitude, and ω_{p} is the modulated driving frequency that is close to the mechanical resonance frequency ω_0 for strong amplitude responses amplified by the mechanical mode. The mechanical response of a single device is then characterized by the measured voltage amplitude recorded in a balanced photodetector while sweeping ω_{p} over the mechanical mode with different values of V_{p} from 1 to 5 V. The results are shown in Fig. 2a in the main text, where the measured voltage amplitude reaches its maximum when $\omega_p \approx \omega_0$ and increases monotonically with V_{RF}. Each measured voltage amplitude values can be calibrated into oscillation displacements in the unit of nanometer, as shown in Fig. 2b in the main text. The calibrated maximum displacement as a function of RF drive shows a linear dependence on the RF drive with a responsivity of 4.4 nm V^{-1}. From this result, the maximum displacement Δz is calculated to be 22 nm at an applied RF drive of 5 V.

We also calculated the dielectric gradient force created by the RF drive to estimate the lattice strain in the vibrating cantilever induced by the mechanical displacement. When applying an RF drive to actuate the cantilever that vibrates in the fundamental out-of-plane flexural mode, the effective dielectric driving force can be estimated by considering the model of a one-dimensional simple harmonic oscillator. The effective mass of such oscillator can be calculated by $m_{eff} = \frac{33}{140}\rho V \approx 29$ pg, where $\rho = 5.5 \times 10^3\ \mathrm{kg\ m^{-3}}$ is the average density of GeSn, and V is the volume of the beam. The effective stiffness is then calculated as $k_{eff} = m_{eff} \cdot (2\pi f)^2 = 10.7\ \mathrm{N\ m^{-1}}$, with the resonance frequency $f = 3.062\ \mathrm{MHz}$ in the present case. At an RF drive of 5 V, the dielectric gradient force applied onto the cantilever is expressed by $F = \frac{k_{eff}}{Q} \Delta z {\sim} 0.24$ nN in which the mechanical factor Q is 1000 and the maximum displacement of the beam $\Delta z {\sim} 22$ nm. By inserting the estimated dielectric gradient force in the FEM simulations, one can estimate the magnitude of the strain and investigate the force-strain relation. As a result, the dielectric gradient force F of 0.48 nN when an RF drive of 10 V is applied, and the cantilever experiences average strain $\Delta\epsilon_{xx}$ of 0.1% in the lower part of the GeSn layer with a linear dependence on the driving force, as shown in Supplementary Fig. 8.

Based on the simulation result above, time-domain mechanical characteristics are analytically investigated. The time-dependent displacement can be expressed as $Z(t) = \Delta z \cdot \cos(\omega_\mathrm{p} t + \varphi)$, where φ is a phase delay between RF drive and mechanical oscillation. The phase delay can be deduced from the motion equation of a driven harmonic oscillator $\ddot{Z} + \frac{\omega_0}{Q}\dot{Z} + {\omega_0}^2 Z = F\sin(\omega_p t)$, which results in $\varphi = tan^{-1}\left[\frac{\omega_0\omega_p}{Q(\omega_p^2 - \omega_0^2)}\right]$. The response function of such a driven harmonic oscillator is depicted in Supplementary Fig. 9. In a resonantly driven oscillator ($\omega_p \approx \omega_0$), the phase delay is calculated to be $\varphi {\sim} -90°$. Owing to the linear dependence on RF drive, both the mechanical displacement Δz and lattice strain $\Delta\epsilon_{xx}$ show a sinusoidal dependence on RF drive with a phase shifted by −90°. The time-dependent lattice strain can be expressed as expressed as $\epsilon_{xx}(t) = \Delta\epsilon_{xx} \cdot \cos(\omega_\mathrm{p} t + \varphi)$, where $\Delta\epsilon_{xx}$ is the average strain of 0.1% at an applied RF drive of 10 V.

Note 6. Finite element method simulation

3D FEM simulations are performed for further investigations of strain in the oscillating cantilever. The model was constructed using the same dimensions as our fabricated structure. The mechanical eigenfrequency of the fundamental out-of-plane flexural mode in such a cantilever is first calculated to be $\omega_{th}/2\pi \sim 3.046$ MHz, in great agreement with the experimental result. The dielectric gradient force is loaded on the oscillating beam, with a value on the order of 0.48 N to mimic the dielectric gradient forces generated by a 10 V RF drive, as estimated in Supplementary Note 5.

Note 7. Influence of mechanical oscillation on laser emission intensity

To investigate the influence of mechanical oscillations on laser emission intensity, we first calculated the maximum bending angle that the oscillator could experience during mechanical actuation. The calculated maximum bending angle is 0.18° with the highest displacement of ~44 nm at an RF drive of 10 V. Based on our finite-difference time-domain (FDTD) simulations, the simulated intensity difference between the oscillators bent by 0° and 0.18° is less than 0.1%, indicating that the mechanical displacement of the oscillator has negligible influence on the laser emission intensity.

Note 8. Influence of RF drive amplitude on the laser emission

To further understand the effect of mechanical motion on the lasing emission, we obtained lasing spectra by sweeping the RF drive amplitude from 0 V to 10 V (Supplementary Fig. 10a). The relative phase is fixed at 270°, at which the lasing medium is under the maximum tensile strain (Fig. 3a in the main text). The three key parameters—wavelength, intensity, and FWHM—of the lasing spectra are plotted in Supplementary Fig. 10b. Under no RF drive, the dominant peak is at ~2266.5 nm, which is the expected value for the oscillator with no mechanical displacement. As the RF drive amplitude is increased, Peak 1 at ~2266.5 nm is gradually shifted to a longer wavelength due to the strain-induced refractive index change, as explained in Fig. 4a in the main text. As the RF drive amplitude is further increased beyond 6 V, Peak 2 emerges at >2303 nm and grows in intensity significantly at larger RF drive amplitudes, which can be attributed to the modified gain spectra under large tensile strain. It should be noted that the existence of a small peak between Peak 1 and Peak 2 can be attributed to the non-uniform distribution of photoexcited carriers in the lasing medium under pulsed laser pumping condition, allowing for the existence of different-order lasing modes[16]. The peak position of this optical mode is largely consistent with the simulation result (Fig. 4c in the main text). The lasing mode at Peak 1 is quenched at larger RF drive amplitudes and disappears at ~10 V. We obtained the coarse-tuning range of ~37.6 nm (equivalent to ~2.2 THz) with the fine-tuning range of ~1 nm (equivalent to ~50 GHz) with a relatively small RF drive of 10 V. It is worth mentioning that the tuning range of our tunable laser can be further increased by using several approaches. One straightforward approach is increasing the mechanical oscillation amplitude, leading to a higher lattice strain in the GeSn gain medium. Since the mechanical oscillation relies on the RF drive, increasing the RF drive voltage can enable achieving a wider coarse-tuning range in our device. Another powerful approach involves enhancing the mechanical Q-factor of our resonantly driven oscillator. Since the enhanced mechanical Q-factor can amplify the mechanical responsivity in response to the RF drive, it allows for achieving higher mechanical oscillation amplitude and therefore higher lattice strain in the gain medium at the same RF drive voltage. The significance of harnessing high Q mechanical resonances for tunable lasers can be further appreciated by referring to the static tuning results with DC bias voltages, where a much higher voltage is required to achieve the same amount of tuning (see more details on the DC-tuning measurements in the next paragraph). Importantly, this improvement in the mechanical *Q*-factor can also result in reduced power consumption for the emission wavelength tuning.

Under the AC-tuning with an RF drive amplitude of 10 V, our resonantly driven nanomechanical oscillator shows the blue-shift of ~0.2 nm at the maximum compressive strain, as shown in Figure 3c (top panel) in the main text. Given the mechanical Q-factor of ~500, achieving the same amount of blue-shift (i.e., ~0.2 nm) with a DC drive requires the application of a 500-time higher DC voltage. In our case, the required DC bias voltage to achieve a ~0.2 nm blue-shift is estimated to be ~3500 V, which is 500 times higher than a root-mean-square voltage of ~7 V corresponding to an RF drive of 10 V. Since applying such a high DC bias voltage is challenging due to an electrical breakdown of the insulator layer underneath the metal electrodes, we reduced the DC bias voltage by approximately one-tenth, which is expected to result in a proportional reduction in the tuning range.

Supplementary Figure 11 presents the result of the DC-tuning measurement at different DC bias voltages. When the DC bias voltage is increased from 0 V to 300 V, the emission wavelength is blue-shifted by ~0.019 nm due to the compressive strain in the gain medium, which largely agrees with our expectation explained in the previous paragraph. Although the tuning range is reduced by one-tenth compared to our AC-tuning, the achieved tuning range is comparable to that enabled by electro-optic tuning mechanisms in nonlinear materials such as lithium niobate, which show the emission tuning of ~0.010 nm[18-20]. This DC-tuning result further demonstrates the pivotal role of leveraging mechanical resonance in nanomechanical oscillators with a high mechanical Q-factor in achieving highly efficient emission tuning.

Note 9. Capacitive effect on the laser emission

To investigate the capacitive effect that can alter the refractive index via charge accumulations and its influence on the laser emission, two additional PL measurements were performed: first with DC bias at different voltages and second with RF drive at different frequencies.

In the first additional PL measurement, we examined the influence of DC bias on laser emission. Supplementary Figure 12a presents laser emission spectra measured at various DC bias voltages. No laser emission wavelength shift is observed across various DC voltages, indicating that charge accumulation induced by DC bias has a negligible influence on the laser emission.

In the second additional PL measurement, we measured the laser emission spectra at different RF drive frequencies, as depicted in Supplementary Fig. 12b. The RF drive voltage and the relative phase between the RF drive and optical pump pulse are fixed at 5 V and 270°, respectively. The emission wavelength is shifted only at 3.15 MHz, which corresponds to the mechanical resonance frequency, while the emission peak position remains the same at any other frequencies. It should be noted that if the charge accumulation by the RF drive would lead to a significant change in the local refractive index in the gain medium, the laser emission spectra should also shift by the applied RF drive regardless of the driving frequencies. However, since the emission wavelength is shifted only at 3.15 MHz, we confirm that the laser emission shift is mainly due to the resonant mechanical oscillation, and the capacitive effect is negligible in our tunable laser.

Note 10. Theoretical modelling for optical gain

Theoretical modelling was conducted for GeSn with a Sn content of 10.6 at% at 4 K. We first calculated the band structure using the 8-band k·p model for the uniaxially strained GeSn ranging from −0.1% to 0.1% strain. The optical gain was then calculated with the assistance of the expressions provided by Chuang[21]. Liu *et al*.[22] were referenced for the Luttinger parameters of the GeSn combination, and the remaining parameters can be found in Rainko *et al*.[23] The optical gain was calculated at fixed carrier injection densities of 2.6×10^{17} cm^{-3} that corresponds to pump power density of 56.9 kW cm^{-2}.

Note 11. Estimation of power consumption in laser tuning

We tune the lasing wavelength by driving the mechanical oscillation of the cantilever using a dielectric driving scheme, which is achieved by applying RF bias to electrodes to generate gradient force that will load on the cantilever. In our device, such a driving system can be modeled as RC circuit (as shown in Supplementary Fig. 13), with a total power dissipation expressed as:

$$P_{in} = P_{elec} + P_{mech}$$

in which P_{elec} or P_{mech} is the electrical power or mechanical power respectively.

The mechanical power dissipation can be estimated simply by:

$$P_{mech} = \langle F \cdot V \rangle = \frac{F \cdot \Delta z \cdot \omega_m}{2}$$

where F is the driving force loaded on the cantilever, Δz is the resulting displacement, and ω_m is the oscillation frequency. We learn from Supplementary Note 5 that, with an RF drive of 10 V, we have $F \sim 0.48$ nN, $\Delta z \sim 44$ nm, and $\omega_m = 2\pi \cdot 3.062$ MHz. This results in $P_{mech} \sim 200$ pW.

To calculate the electrical power P_{elec}, we estimate the impedance of the RC circuit by:

$$Z(\omega) = \frac{R_{sub}}{1 + i\omega C R_{sub}}$$

We measured the I-V characteristics of the device and found R_{sub} is on the order of $10^{12}\Omega$. The two electrodes can be considered as operating as even mode capacitance of a slot line of length L, and therefore the capacitance of the circuit can be estimated by[24]:

$$C \approx \frac{\epsilon_0(\epsilon + 1)}{2} L$$

where ϵ_0 is the vacuum permittivity, $\epsilon \sim 4$ is the relative permittivity of the substrate, and $L \sim 20$ μm is the length of the electrode. As a result, we obtain a capacitance C about 4×10^{-16} F. Then we obtain the impedance $Z(\omega) \approx 1.6 \cdot 10^4 - i \cdot 1.3 \cdot 10^8 \Omega$. Eventually we can calculate the electrical power dissipation when driving by a 10V RF bias:

$$P_{elec} = \frac{V^2 Re(Z)}{2 \cdot |Z|^2} \sim 50\ pW$$

The above estimation reveals that not only P_{elec} and P_{mech} are of similar magnitude, but also the mechanical dissipation is significantly higher than the electrical dissipation of the modulator. This suggests that, in the system, the mechanical dissipation (corresponding to an effective "mechanical resistance" R_m) is highly efficient as compared to the dissipation to the substrate (which corresponds to R_{sub}). As a result, the mechanical oscillation can modify substantially the impedance of the entire system, and thus we need to consider R_m to accurately estimate the total power dissipation P_{in}.

To provide such estimation, we first use the fact that any mechanical resonator can be identically mapped into an electrical LRC circuit. Furthermore, as shown in Supplementary Note 5, the driving force F is proportional to the bias applied on the capacitor C. Therefore, we can regard the mechanical oscillator as a LRC circuit that is parallel with the capacitor (see Supplementary Fig. 14). When at resonance, the reactive effects of the inductor and capacitor cancel each other out, resulting in a purely resistive circuit where $P_{mech} = \frac{V^2}{2R_m}$. Thus, from the previous calculation of P_{mech}~200 pW, we can extract the effective mechanical resistance R_m~0.25 TΩ. This resistance is in parallel with the R_{sub}~1 TΩ, thus the entire system can be sketched as Supplementary Fig. 15 where the total resistance of the system is R_{eff}~0.2 TΩ. We then can calculate the impedance of the RC circuit again but this time with R_{eff} and obtain $Z(\omega) \approx 8 \cdot 10^4 - i \cdot 1.3 \cdot 10^8\ \Omega$.

Eventually, we calculate again the electrical dissipation:

$$P_{in} = \frac{V^2 Re(Z)}{2 \cdot |Z|^2} \sim 240\ pW$$

which is very similar to the mechanical dissipation P_{mech}~200 pW. Indeed, in that case the "mechanical" resistance is much smaller than the leakage through the substrate, and only the mechanical dissipation dominates our system. This further indicates that our modulation scheme operates with very high efficiency, as 200/240≈83% of the injected RF power is effectively used for the modulation function. Note that, a possible way to cancel further the effect of the substrate resistance R_{sub} and render the system nearly 100% effective would be to etch a trench between the two electrodes.

Note 12. Approaches to increase oscillation frequency

The mechanical oscillation frequency of the nanobeam can be estimated based on the Euler-Bernoulli theory[25]. This theory allows to solve the equation of motion and calculate the flexural vibration frequencies of a nanobeam. The equation is as follows:

$$f = \frac{C}{2\pi}\sqrt{\frac{E}{12\rho}}\frac{u}{l^2}$$

Here, E represents the Young's modulus, ρ is the material density, and u and l denote the thickness and length of the oscillating beam, respectively. The constant C is associated with the fundamental flexural mode and equals 3.5 for a cantilever structure.

There are various methods that can be employed to increase the oscillation frequency. One straightforward approach is to change the design parameters such as increasing the thickness u and reducing the length l of the GeSn nanobeam. Alternatively, employing a doubly-clamped nanobeam, which increases the value of constant C to 22.4, can also increase the oscillation frequency. Another effective technique is to introduce a static strain into the current device structure, which increases the stiffness of the nanobeam, resulting in a higher oscillation frequency[26]. Additionally, it is also possible to achieve higher oscillation frequency by utilizing higher-order modes of mechanical oscillation, as demonstrated in a reference[27].

Supplementary Figures

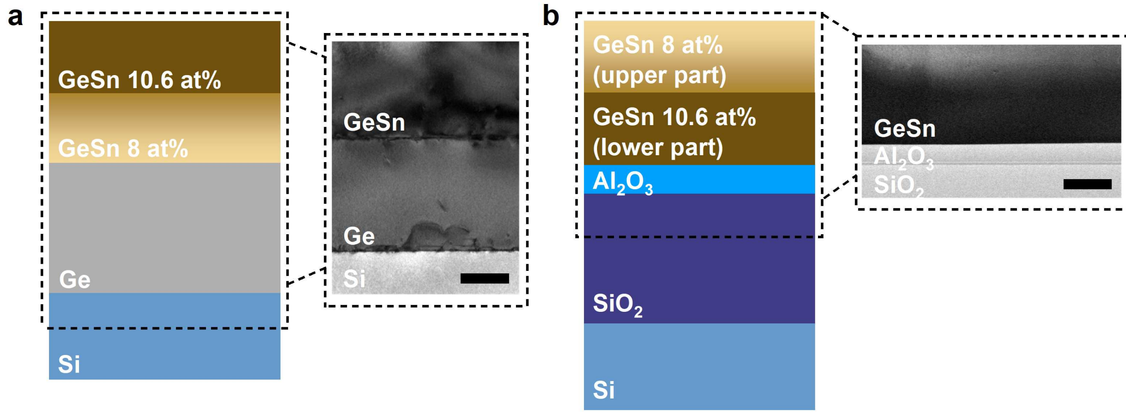

Supplementary Figure 1 | GeSn material characterization. Cross-sectional schematics of the material stack for the **a,** as-grown GeSn and **b,** GeSnOI substrates. The cross-sectional TEM images of each substrate are shown in the inset. Scale bars, 450 nm (**a**)**,** 400 nm (**b**).

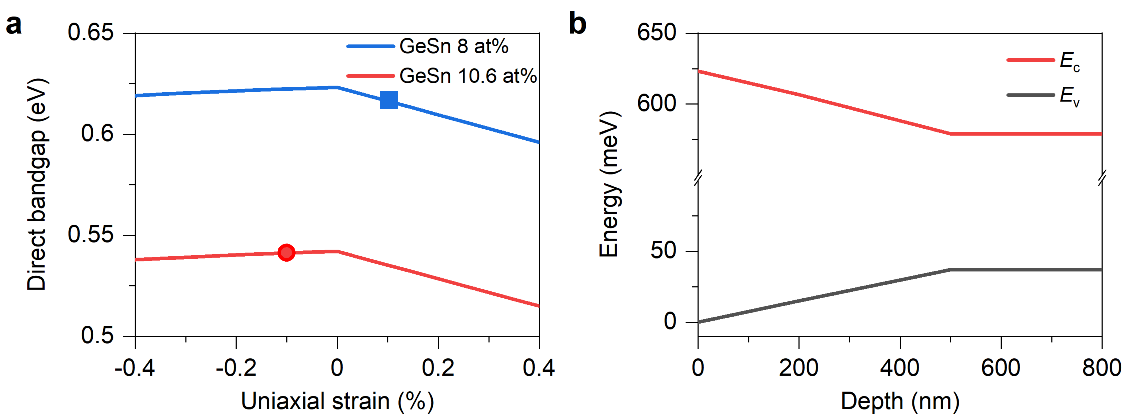

Supplementary Figure 2 | a, Calculated bandgap of the GeSn layers with Sn contents of 8 at% and 10.6 at% as a function of uniaxial strain at 4 K. **b,** Calculated band diagram of the compositionally graded GeSn layer along the sample depth direction.

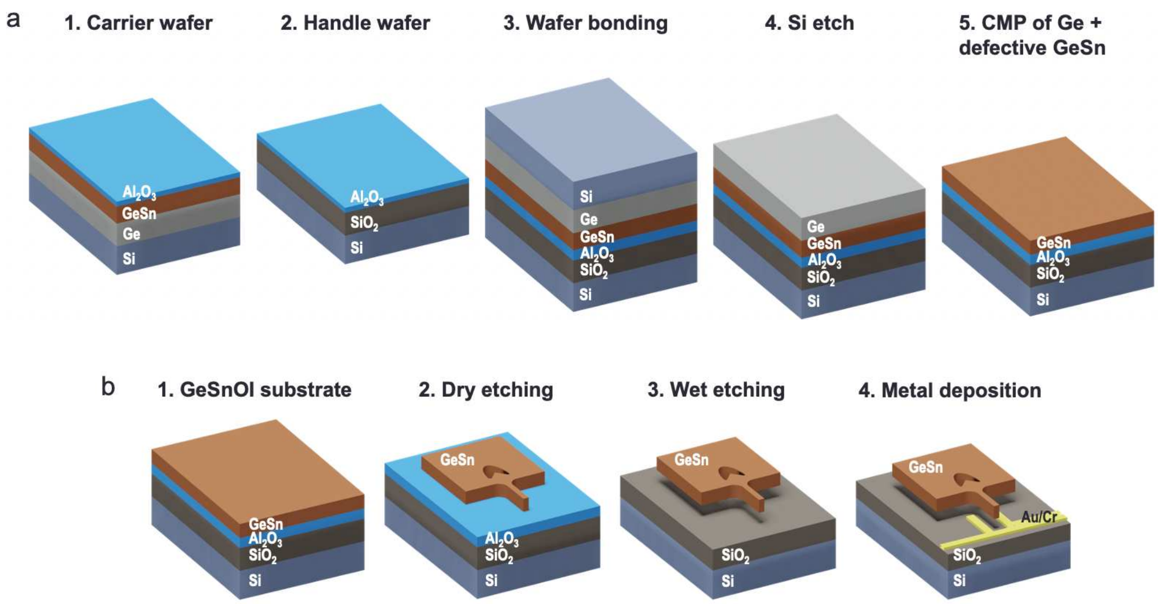

Supplementary Figure 3 | Fabrication procedures. a, Bonding process used to produce the GeSnOI substrate. **b,** Fabrication process of a GeSn oscillator.

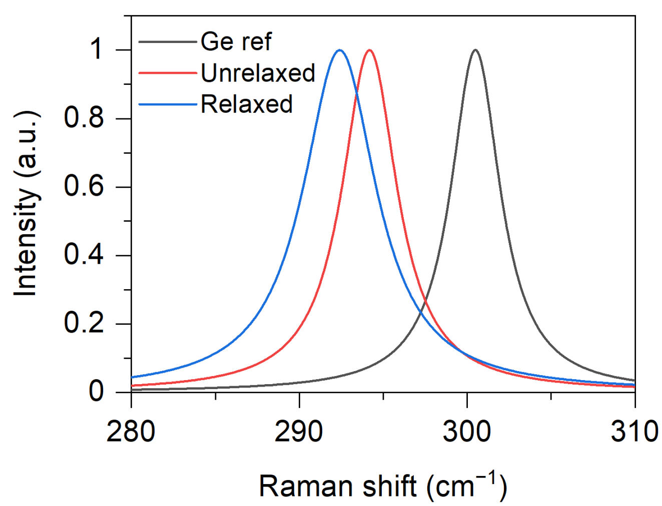

Supplementary Figure 4 | Raman spectroscopy showing the relaxation of the residual compressive strain in the GeSn cantilever after wet etching process. A bulk Ge substrate is measured for reference.

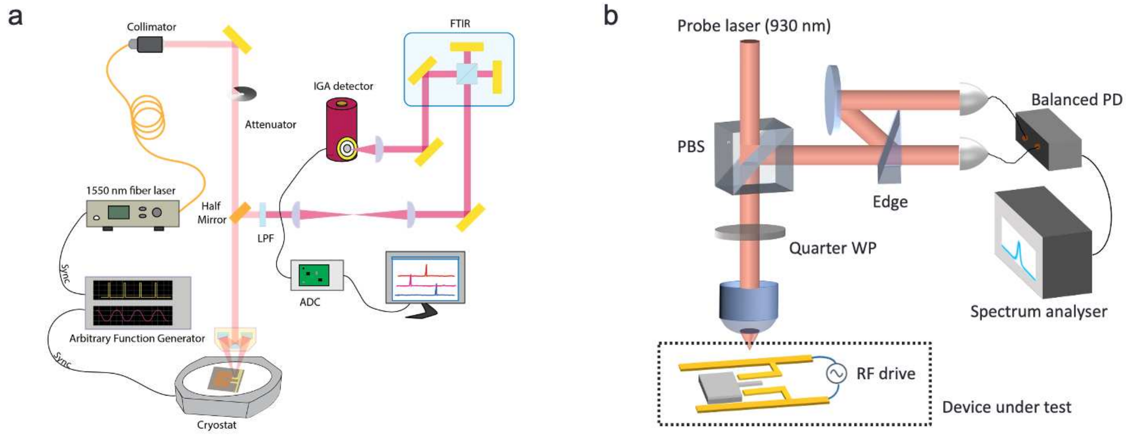

Supplementary Figure 5 | Experimental setups. Schematics showing the **a,** PL and **b,** mechanical measurement setups.

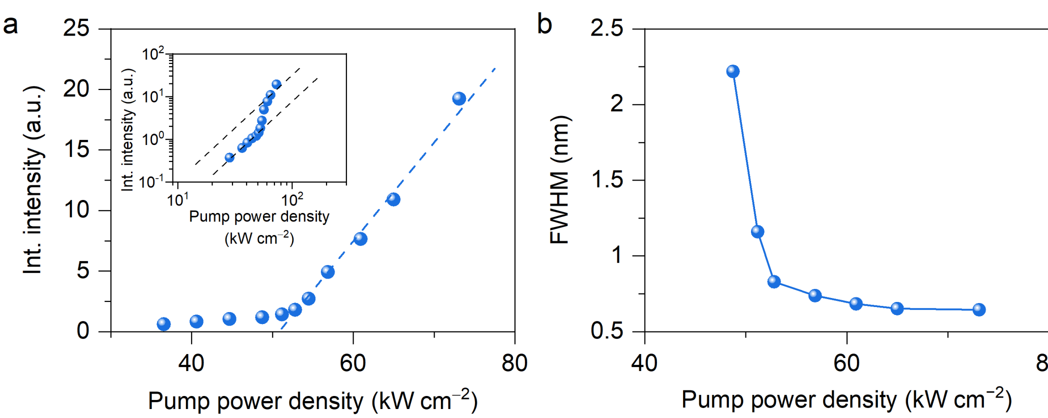

Supplementary Figure 6 | Lasing characteristics. a, L-L characteristics of the fabricated cantilever-type GeSn laser at 4K. **b,** FWHM as a function of pump power density for the same device.

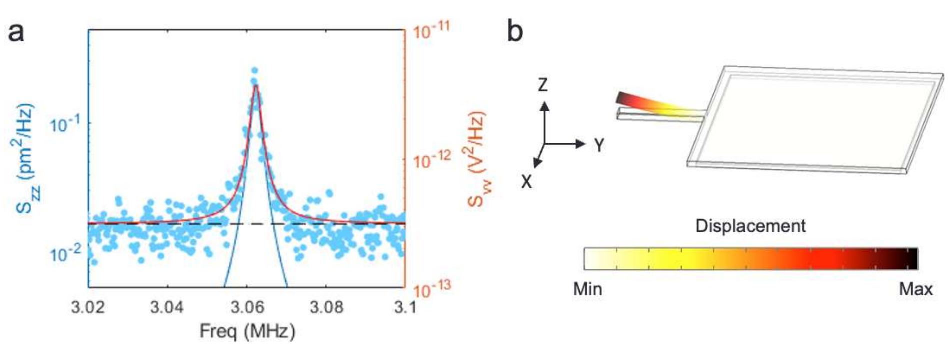

Supplementary Figure 7 | Mechanical characterization and calibration. a, The experimental Brownian motion spectrum (blue dots, measured with 200 Hz resolution bandwidth) can be well fitted by the red curve, which is a sum of a Lorentzian distribution (blue solid line) and a noise floor (black dashed line). By relating this spectrum to the thermal noise $k_B T$, one can convert the voltage power spectral density S_{vv} (right y-axis) to the motion power spectral density S_{zz} (left y-axis). **b,** FEM simulation of the fundamental out-of-plane flexural vibration mode to visualize the mechanical displacement.

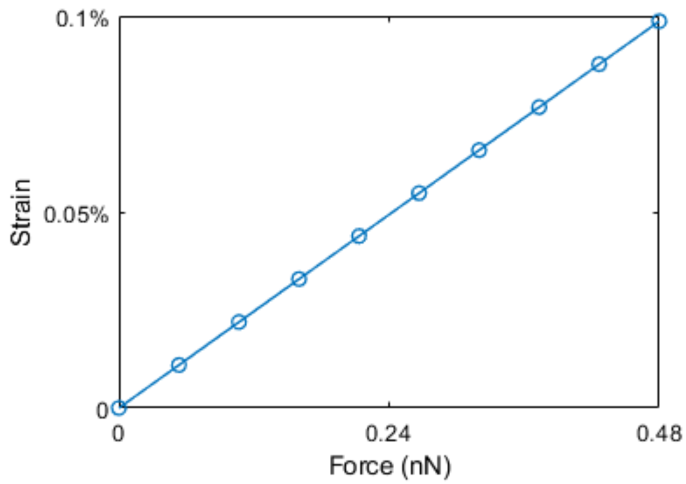

Supplementary Figure 8 | Force-dependent FEM simulation result revealing that the strain induced by mechanical oscillation is linearly dependent on the driving force.

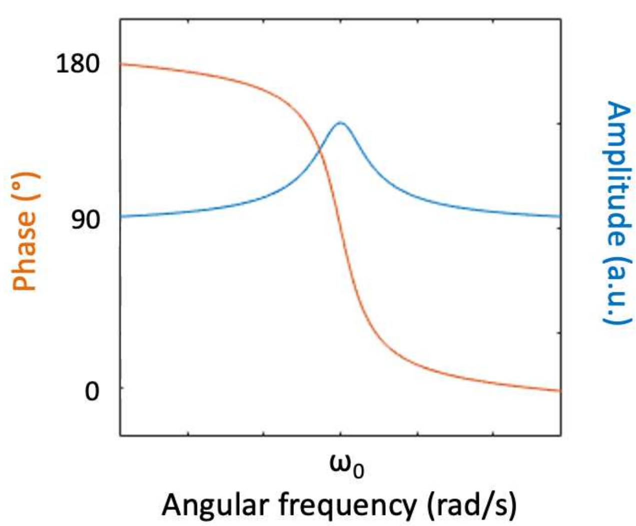

Supplementary Figure 9 | The mechanical response function of the driven harmonic oscillator.

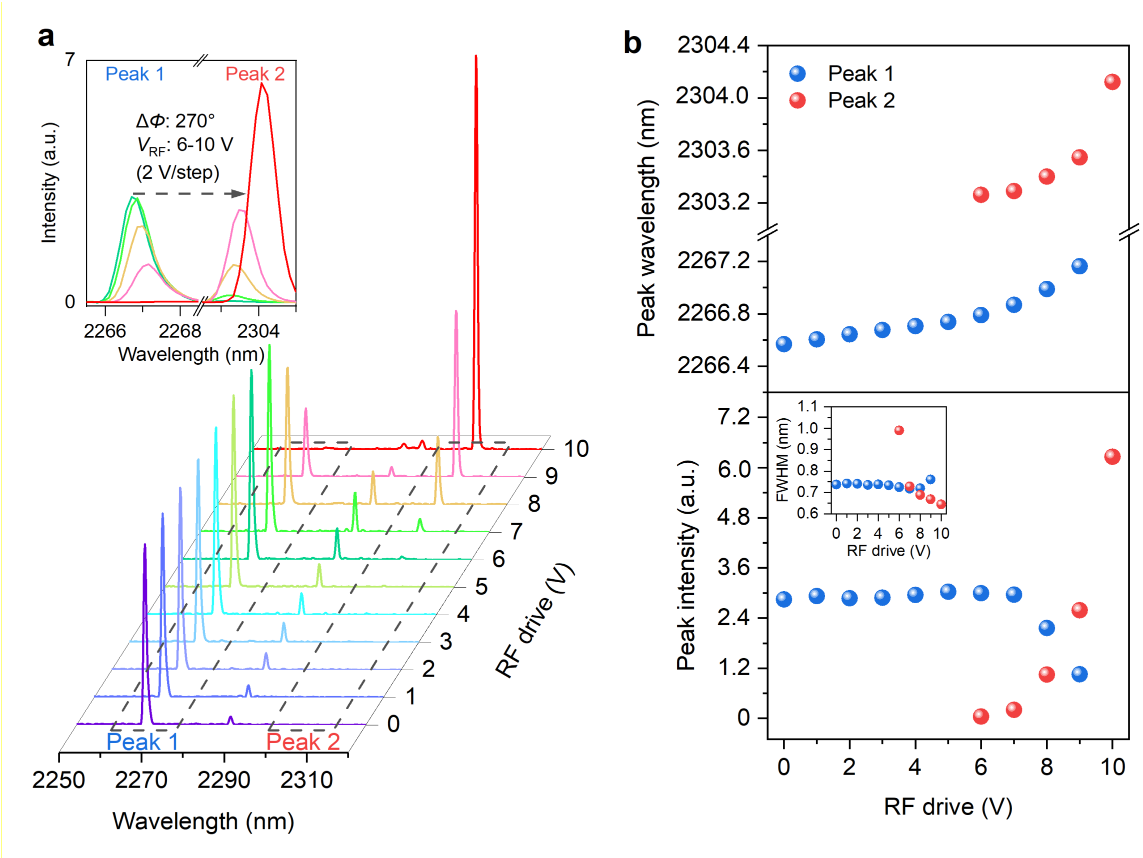

Supplementary Figure 10 | Influence of RF drive amplitude on the laser emission and performance comparison. a, Lasing spectra measured under different amplitudes of RF drive from 0 V to 10 V with a 1 V/step. The relative phase Δ*Φ* is fixed at 270°. Inset: magnified lasing spectra of Peak 1 and Peak 2 at RF drive V_{RF} = 6-10 V. **b,** Extracted emission wavelength (top), intensity (bottom), and FWHM (inset) as a function of the applied RF drive for Peak 1 and Peak 2. A continuous and wide-range tuning is observed as the applied RF drive is increased.

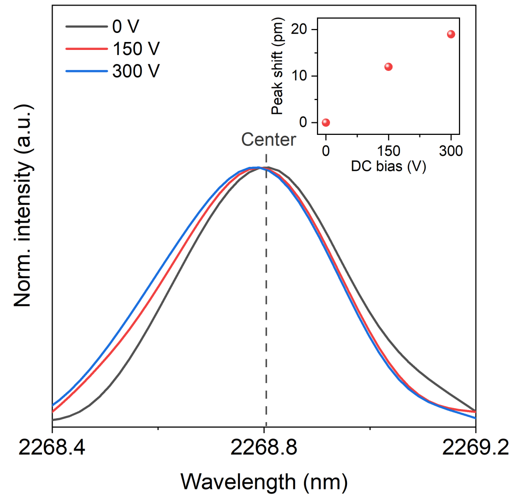

Supplementary Figure 11 | Normalized laser emission spectra at various high DC bias voltages. Inset: The amount of the emission peak shift as a function of the DC bias voltage.

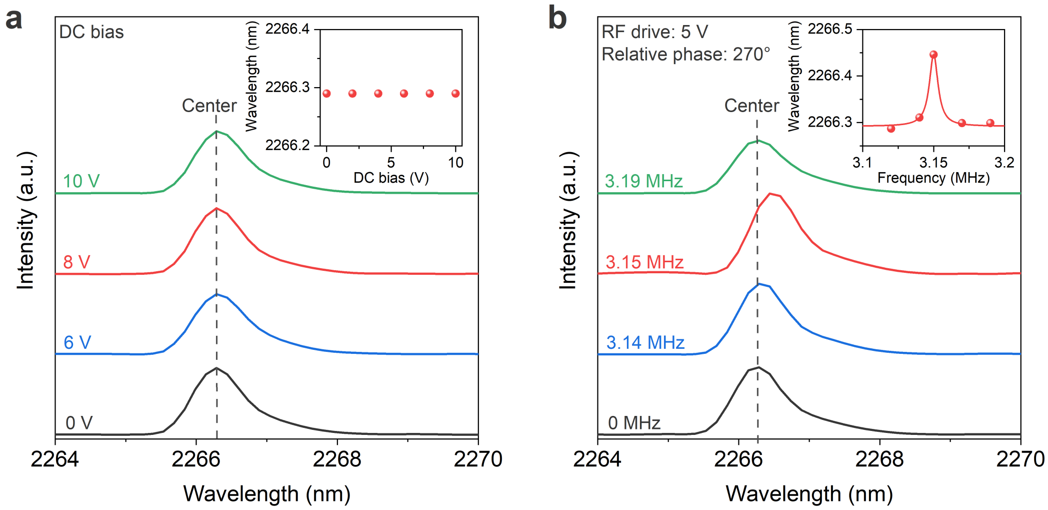

Supplementary Figure 12 | a, DC bias voltage-dependent laser spectra of the oscillator. Inset: peak emission wavelength as a function of the DC voltage. No laser emission shift is observed under any DC bias. **b,** RF drive frequency-dependent laser spectra of the oscillator. Inset: peak emission wavelength as a function of RF drive frequency. The lasing peak is shifted only when the RF drive frequency is synced to the mechanical resonance frequency of 3.15 MHz.

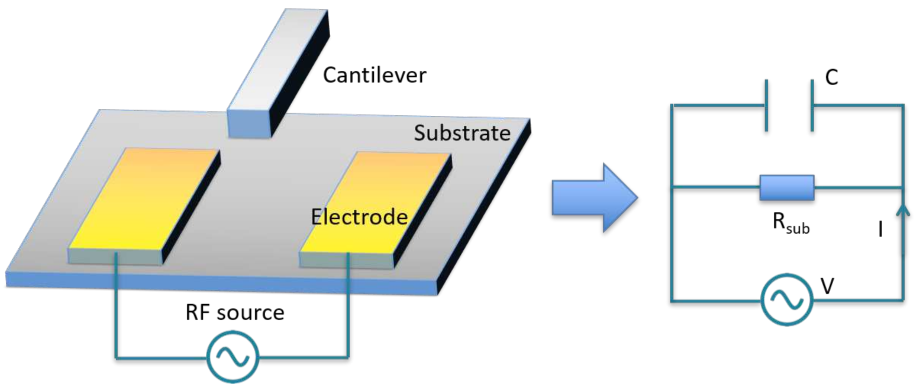

Supplementary Figure 13 | Equivalent electrical circuit of the system.

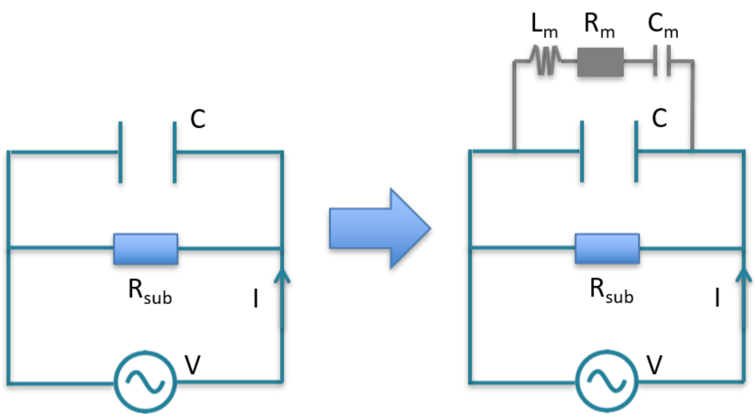

Supplementary Figure 14 | Equivalent electrical circuit of the system considering mechanical impedance.

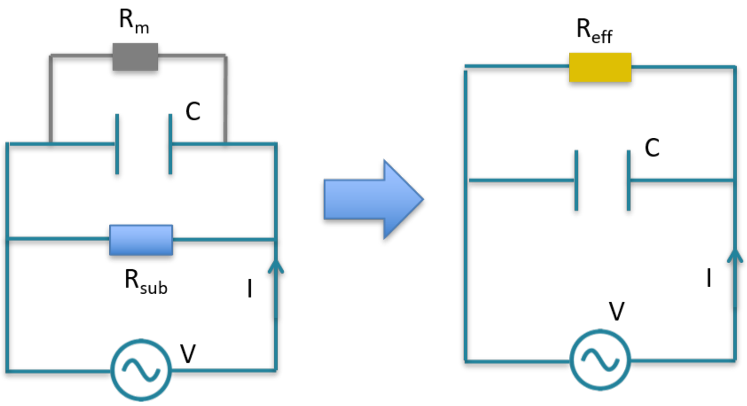

Supplementary Figure 15 | Equivalent electrical circuit of the system at resonance.

Supplementary Table

Ref.	Tuning mechanism	Coarse-tuning range (nm) [in frequency]	Fine-tuning range (nm) [in frequency]	Power consumption for wavelength tuning (nW)	Tuning efficiency (nm/nW) [in frequency]
3	Thermal	12.5 [6.1 THz]	0.07 [33.9 GHz]	6.0×10^{7}	2.08×10^{-7} [1.02×10^{-7} THz/nW]
25	Thermal	43 [4.6 THz]	2.5 [270 GHz]	3.4×10^{7}	1.26×10^{-6} [1.35×10^{-7} THz/nW]
26	Thermal	38 [4.5 THz]	N/A	2.6×10^{7}	1.46×10^{-6} [1.73×10^{-7} THz/nW]
6	MEMS	N/A	18 [7.4 THz]	100	0.18 [0.07 THz/nW]
27	MEMS	N/A	2.5 [1.02 THz]	50	0.05 [0.02 THz/nW]
9	Electro-optic	35 [4.4 THz]	1.7 [212 GHz]	1.0×10^{7}	3.50×10^{-6} [4.4×10^{-7} THz/nW]
10	Electro-optic	34 [4.3 THz]	N/A	2.8×10^{6}	1.21×10^{-5} [1.5×10^{-6} THz/nW]
This work	NEMS oscillator	37.6 [2.2 THz]	1 [50 GHz]	0.24	156.67 [9.17 THz/nW]

Supplementary Table 1 | Summary of performance metrics of various tunable lasers using thermal heater, MEMS cavity, electro-optic, and nanomechanical oscillator (this work). The reference numbers in Supplementary Table 1 correspond to the ones in the main text. The power consumption values in Table 1 are benchmarked only for the emission wavelength tuning, rather than the overall power consumption of the entire laser operation, since the lasers in Table 1 work under different operation schemes with respect to pumping and temperature. By focusing on this aspect of the tuning power consumption, we aim to provide valuable insights into the intrinsic emission tuning performance of various tuning mechanisms.

References

1. Unterreithmeier, Q. P., Weig, E. M. & Kotthaus, J. P. Universal transduction scheme for nanomechanical systems based on dielectric forces. *Nature* **458**, 1001-1004 (2009).
2. Liu, J. *et al.* Nonlinear oscillation states of optomechanical resonator for reconfigurable light-compatible logic functions. *Advanced Optical Materials*, 2202133 (2022).
3. Liu, J. *et al.* Ultrafast detection of terahertz radiation with miniaturized optomechanical resonator driven by dielectric driving force. *ACS Photonics* **9**, 1541-1546 (2022).
4. Burt, D. *et al.* Direct bandgap GeSn nanowires enabled with ultrahigh tension from harnessing intrinsic compressive strain. *Applied Physics Letters* **120**, 202103 (2022).
5. Jung, Y. *et al.* Optically pumped low-threshold microdisk lasers on a GeSn-on-insulator substrate with reduced defect density. *Photon. Res.* **10**, 1332-1337 (2022).
6. Gupta, S., Magyari-Köpe, B., Nishi, Y. & Saraswat, K. C. Achieving direct band gap in germanium through integration of Sn alloying and external strain. *Journal of Applied Physics* **113**, 073707 (2013).
7. Nam, D. *et al.* Strain-Induced Pseudoheterostructure Nanowires Confining Carriers at Room Temperature with Nanoscale-Tunable Band Profiles. *Nano Letters* **13**, 3118-3123 (2013).
8. Dou, W. *et al.* Optically pumped lasing at 3 μm from compositionally graded GeSn with tin up to 22.3%. *Opt. Lett.* **43**, 4558-4561 (2018).
9. Chinn, S. R., Zory, P. S. & Reisinger, A. R. A model for GRIN-SCH-SQW diode lasers. *IEEE Journal of Quantum Electronics* **24**, 2191-2214 (1988).
10. Tsang, W. T. Extremely low threshold (AlGa)As graded-index waveguide separate-confinement heterostructure lasers grown by molecular beam epitaxy. *Applied Physics Letters* **40**, 217-219 (1982).
11. Joo, H.-J. *et al.* 1D photonic crystal direct bandgap GeSn-on-insulator laser. *Applied Physics Letters* **119**, 201101 (2021).
12. Gassenq, A. *et al.* Raman spectral shift versus strain and composition in GeSn layers with 6%–15% Sn content. *Applied Physics Letters* **110**, 112101 (2017).
13. Wirths, S. *et al.* Lasing in direct-bandgap GeSn alloy grown on Si. *Nature Photonics* **9**, 88-92 (2015).
14. Wang, B. *et al.* GeSnOI mid-infrared laser technology. *Light: Science & Applications* **10**, 232 (2021).
15. Kim, Y. *et al.* Enhanced GeSn Microdisk Lasers Directly Released on Si. *Advanced Optical Materials* **10**, 2101213 (2022).
16. Elbaz, A. *et al.* Ultra-low-threshold continuous-wave and pulsed lasing in tensile-strained GeSn alloys. *Nature Photonics* **14**, 375-382 (2020).
17. Cleland, A. N. & Roukes, M. L. Noise processes in nanomechanical resonators. *Journal of Applied Physics* **92**, 2758-2769 (2002).
18. Snigirev, V. *et al.* Ultrafast tunable lasers using lithium niobate integrated photonics. *Nature* **615**, 411-417 (2023).
19. Li, M. *et al.* Integrated Pockels laser. *Nature Communications* **13**, 5344 (2022).
20. Minet, Y., Herr, S. J., Breunig, I., Zappe, H. & Buse, K. Electro-optically tunable single-frequency lasing from neodymium-doped lithium niobate microresonators. *Opt. Express* **30**, 28335-28344 (2022).
21. Chuang, S. L. *Physics of photonic devices* (Wiley New York, 2009).
22. Liu, S.-Q. & Yen, S.-T. Extraction of eight-band k · p parameters from empirical pseudopotentials for GeSn. *Journal of Applied Physics* **125**, 245701 (2019).
23. Rainko, D. *et al.* Investigation of carrier confinement in direct bandgap GeSn/SiGeSn 2D and 0D heterostructures. *Scientific Reports* **8**, 15557 (2018).

24. Bahl, I. J. Lumped elements for RF and microwave circuits. *Artech House microwave library, Boston London* (2003).
25. Cleland, A. N. Foundations of Nanomechanics (Springer-Verlag, New York, 2003).
26. Sazonova, V. *et al.* A tunable carbon nanotube electromechanical oscillator. *Nature* **431**, 284-287 (2004).
27. Gaidarzhy, A., Zolfagharkhani, G., Badzey, R. L. & Mohanty, P. Spectral response of a gigahertz-range nanomechanical oscillator. *Applied Physics Letters* **86**, 254103 (2005).